Measurement of Hydrodynamic Growth near Peak Velocity in an Inertial Confinement Fusion Capsule Implosion using a Self-Radiography Technique

L. A. Pickworth,[1,*] B. A. Hammel,[1] V. A. Smalyuk,[1] A. G. MacPhee,[1] H. A. Scott,[1] H. F. Robey,[1] O. L. Landen,[1] M. A. Barrios,[1] S. P. Regan,[2] M. B. Schneider,[1] M. Hoppe, Jr.,[3] T. Kohut,[1] D. Holunga,[1] C. Walters,[1] B. Haid,[1] and M. Dayton[1]

[1]*Lawrence Livermore National Laboratory, P.O. Box 808, Livermore, California 94551-0808, USA*

[2]*University of Rochester, Laboratory for Laser Energetics, Rochester, New York, USA*

[3]*General Atomics, San Diego, California, USA*

(Received 3 February 2016; published 11 July 2016)

First measurements of hydrodynamic growth near peak implosion velocity in an inertial confinement fusion (ICF) implosion at the National Ignition Facility were obtained using a self-radiographing technique and a preimposed Legendre mode 40, $\lambda = 140$ μm, sinusoidal perturbation. These are the first measurements of the total growth at the most unstable mode from acceleration Rayleigh-Taylor achieved in any ICF experiment to date, showing growth of the areal density perturbation of ~7000×. Measurements were made at convergences of ~5 to ~10× at both the waist and pole of the capsule, demonstrating simultaneous measurements of the growth factors from both lines of sight. The areal density growth factors are an order of magnitude larger than prior experimental measurements and differed by ~2× between the waist and the pole, showing asymmetry in the measured growth factors. These new measurements significantly advance our ability to diagnose perturbations detrimental to ICF implosions, uniquely intersecting the change from an accelerating to decelerating shell, with multiple simultaneous angular views.

DOI: 10.1103/PhysRevLett.117.035001

The goal of inertial confinement fusion (ICF) [1–3] is to implode a spherical target, achieving high compression of a cryogenic deuterium-tritium (DT) fuel layer and high temperature in the central hot spot, triggering ignition and producing significant thermonuclear energy gain.

Ignition-relevant fuel areal densities (ρR) and implosion velocities have been achieved [4,5] in recent experiments at the National Ignition Facility (NIF) [6]. While these key performance parameters were close to the goal of the ignition point design [7], the temperatures and neutron yields were significantly lower than expectations from simulations [4,5]. The poor performance correlated with the amount of plastic shell mixed into the DT hot spot as a result of hydrodynamic instability growth [8–10].

Hydrodynamic instabilities, including Rayleigh-Taylor [11,12], Richtmyer-Meshkov [13–18], and Kelvin-Helmholtz [19–23] play a central role in the performance degradation of spherical implosions in ICF [2,3]. As the shell accelerates, ablation-front perturbations feed through the shell, seeding perturbations on the inner surface, which then grow as the shell decelerates. In addition, the perturbations will grow due to Bell-Plesset [24,25] convergent effects throughout the compression.

Several experimental platforms have been developed to measure instability growth and mix in ignition-relevant conditions on NIF. To date, the measurements made have been at low convergence (<4×) during the acceleration phase, limiting the measured growth of the ρR perturbations to ~550× [26–29]. The experiments use a reentrant cone, allowing only one side of the capsule shell to be radiographed. The measurement of growth from large-amplitude, two-dimensional (2D) preimposed modulations [26–30] showed that the measured instability growth was modeled well with 2D simulations [27–31]. However, "native" 3D roughness measurements highlighted unexpected growth hypothesized to be from the target construction procedures [32–34] and oxygen contamination [35].

Higher convergence measurements of ρR perturbations are challenging and require a different method to radiograph the shell, as a reentrant cone will strongly perturb the implosion [27]. The first ρR modulation measurements near peak convergence were acquired in a direct drive configuration [36–40] at the OMEGA [41] laser facility. The capsule shell included Ti-doped layers that acted as a spectroscopic diagnostic [38–40,42]. At peak compression the hot, compressed core and inner surface of the shell produce bright continuum x-ray emission. This emission is used to self-radiograph the outer, colder shell. Both time-integrated and time-resolved imaging of the implosion at photon energies above and below the dopant K-absorption edge were made [40,43,44]. The technique was extended to take advantage of the more sensitive $1s$-$2p$ absorption [45–47], improving the accuracy of the inferred ρR. Recent work using a multiple pinhole imaging spectrometer [42,48–51] used diagnostic doping of the capsule gas fill [52] to determine hot spot temperature and shell density asymmetries, providing a measurement of total mix in the direct drive implosion.

Measurements when the capsule is fully converged, however, have limitations. Rayleigh-Taylor growth from both acceleration and deceleration, as well as low Legendre mode asymmetries from the drive contribute to the observed ρR perturbations, making interpretation of their origin difficult. Additionally, at peak convergence (PC) the spatial resolution of imaging systems limits the modes that can be resolved to <10, far below the modes measured to be most unstable [26–29,31]. In the work described here, we use the self-radiograph method, but we have enhanced the self-emission at earlier times in the implosion to measure the perturbation from the most unstable mode for our capsule (simulations for this experiment predict mode 45 is at the peak of the growth factor curve [53]) and drive configuration, at peak velocity [53].

Near peak velocity (PV) measurement of the ρR perturbation has the significant advantage that it reflects the integrity of the capsule after the inward acceleration growth is complete. At this time, the capsule is still large enough to measure perturbations with mode ~40, which is at or near peak of the growth factor curve. To achieve sufficient x-ray brightness for a self-radiograph at PV, we add 1% Ar to the gas fill of the capsule. This significantly enhances (~10×) the self-emission over nominal gas fills during the time when the rebounding shock is expanding from the capsule center to meet the incoming shell. Measurements at this time will allow us to infer the cold shell ρR perturbations resulting from native capsule surface roughness and isolated defects as it converges through PV. The enhanced emission from this amount of Ar is sufficient to cool the hot spot during the compression phase and alter the final compression; however, our measurements focus on the times near PV before this perturbation is significant.

This Letter presents the first measurements, using a novel technique, of the total acceleration-phase Rayleigh-Taylor growth, at the most unstable mode, in an ICF experiment. In simulations, a small amplitude mode 40 ρR perturbation that stays in the linear growth regime would grow by a factor of 12 000. Our machined ripple perturbation grows by 7000×, entering saturation as it approaches PV [54]. We believe these measurements to be the highest growth inferred in any ICF implosion experiment to date.

Although our ultimate objective is to observe a snapshot of the total growth arising from the native perturbations at the surface of the capsule, we initially chose to qualify the technique with a known perturbation that would be measurable at the time of the peak self-emission from the rebounding shock. A mode 40 ($\lambda = 140\,\mu$m) sinusoidal ripple, with a (220 ± 20) nm (peak-valley) amplitude (the smallest amplitude possible by current fabrication methods), was machined into the ablator surface. In order to machine the ripple a (3 ± 0.15) μm deep band is cut into the capsule to ensure symmetry. For future experiments it is desirable to remove this feature as it significantly perturbs the implosion after PV. By applying a known perturbation

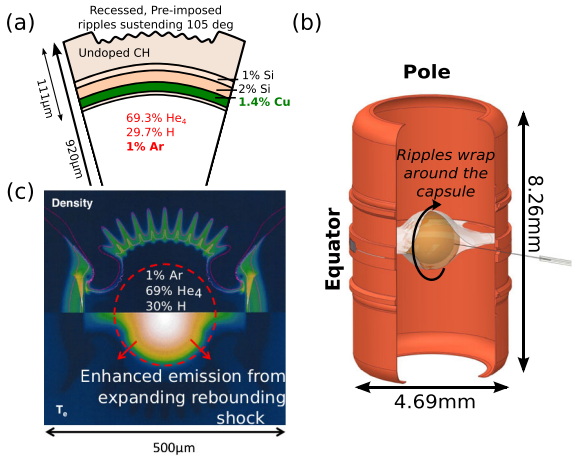

FIG. 1. (a) A pie diagram of the plastic (CH) capsule, doped with Si and 1.4% Cu. A mode 40 sinusoidal ripple is machined into the ablator with a (220 ± 20) nm peak to valley amplitude, recessed 3 μm. (b) Cut away diagram of the Au hohlraum showing the pole, equator, and the orientation of the ripples on the capsule. The ripples are visible on both the polar and equatorial imaging systems. The spectrometer views the unperturbed region on the equator perpendicular to the imaging system. (c) HYDRA [55] simulation ~350 ps before peak compression. When the shock rebounds through the capsule gas fill, the presence of 1% Ar enhances the T_e and, in turn, the self-emission.

with a mode number at the peak of the simulated growth factor spectrum we are measuring the maximum growth that should occur during the acceleration phase. Future experiments will separately examine the final perturbation from different initial seeds, including native surface roughness.

A schematic of the shell dopant and gas fill is shown in Fig. 1(a), indicating the position of the mode 40 ripple on the ablator surface that wraps 360° over the pole of the capsule. The ripple orientation allows diagnostic views through both the perturbed (2D imaging) and unperturbed (spectrometry) regions of the shell. The Ar dopant in the capsule gas required the target to be fielded at 75 K to avoid condensation of the Ar. An inner layer of the capsule ablator was doped with 1.4% Cu for radiographic contrast and as a spectroscopic diagnostic, Fig. 1(a). The depth of the Cu-doped layer was chosen so that it remains unablated at PV in simulations.

The temporal and spectral characteristics of the x-ray emission from the capsule, shown in Fig. 2(a), are diagnosed by a time resolved spectrometer [56,57]. This instrument observes the capsule along a line of sight that does not intercept the ripple. The enhanced self-emission (bremsstrahlung) from the addition of the Ar peaks ~350 ps prior to PC, coincident with PV. This provides a time window in which a series of self-radiographs can be taken using a 2D x-ray imaging system observing along a line of sight through the ripple, Fig. 3. The 1.4% Cu dopant in the shell produces a K-edge absorption feature (8.9 keV),

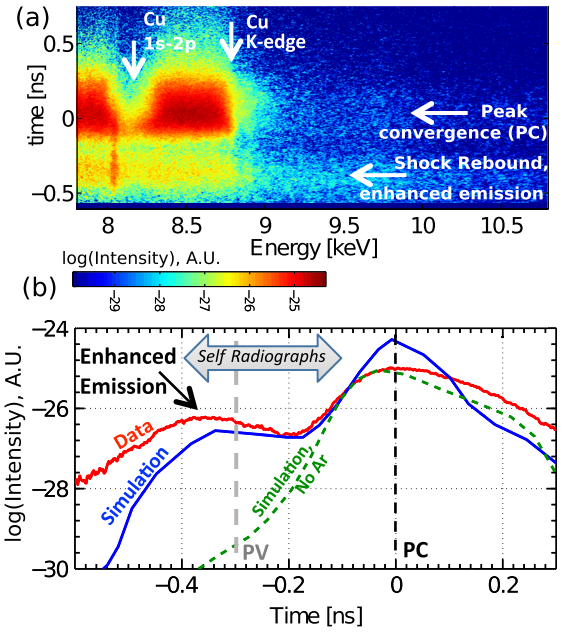

FIG. 2. (a) Time resolved spectrum covering ~1 ns around peak compression (PC, $t = 0$ ps). Absorption features from the Cu dopant in the shell are visible both in the rebounding shock spectrum and at PC. (b) Spectrally integrated emission in a ~1 keV bandpass (8–9.2 keV) in time, showing significantly increased emission ~350 ps prior to PC. This is compared to 1D non-LTE results (blue), showing good agreement in the timing of the self-emission enhancement. For reference, the simulated emission without added Ar is shown (green, dashed).

visible in the spectrum shown in Fig. 2(a). The emission enhancement in the time resolved spectrum is easily visible in Fig. 2(a), and the time history of the capsule self-emission below the Cu K edge is shown in Fig. 2(b).

Capsule-only 2D simulations were performed using a radiation hydrodynamics code, HYDRA [55] to predict the growth of the preimposed modulations. Simulated radiographs, from the transmitted self-emission, were produced to compare to the experimental measurements. These simulations were run assuming local thermodynamic equilibrium (LTE) atomic physics. In addition, 1D non-LTE simulations were performed to predict the self-emission enhancement from the addition of Ar. The electron temperature and density maps from the 2D simulation are shown in Fig. 1(c). The measured emission below the Cu K edge is compared to the simulations in Fig. 2(b) both with and without the Ar dopant. The simulations with Ar predict the general features of the emission, and, in particular, the enhanced self-emission in the shock-rebound phase prior to the PC emission. Figure 1(c) shows a prediction of the perturbation in the shell when the capsule is at a convergence of 6.1×, ($R \sim 150$ μm). From the ratio of the transmitted emission above and below the Cu K edge we can infer the ρR of the Cu, and therefore the shell compression, from the time resolved spectrum shown in Fig. 2. The compression of the shell is given by $\sqrt{\rho_0 R_0/\rho R}$.

We infer a dopant ρR of $(5.7 \pm 0.4) \times 10^{-3}$ g/cm^2, 350 ps prior to PC, giving a capsule convergence of $(5.1 \pm 0.2)\times$ at the time of peak self-emission from the rebounding shock, when the self radiographs will be taken. The cold opacity of Cu was used [58] to infer the compression of the dopant over a 100 ps time average portion of the spectrum. The addition of the Cu dopant creates two additional features in the spectrum shown, $1s$-$2p$ absorption later in time and K-alpha emission throughout.

The ripples on the capsule were oriented as shown in Fig. 1(b), allowing them to be observed by gated x-ray detectors (GXD) [59,60] situated on polar and equatorial lines of sight. These diagnostics consist of a pinhole imaging system coupled to a gated microchannel plate (MCP) x-ray detector and captured 2D self-emission images of the implosion. Each GXD provided a large number of images spanning the period between PC −400 and −100 ps that coincides with the enhanced self-emission. Figure 3 shows three images from each of the polar and equatorial GXDs.

The images are observed though a 10 μm Cu filter which provided a moderately narrow band photon energy response allowing a modulation in optical depth (OD) of the shell to be found. The equatorial and polar detectors are co-timed, allowing a simultaneous measurement. The assumption is made that the emission from the rebounding shock is smoothly varying. The size of the images shown correspond to the size of the emission from the rebounding shock, which is smaller than the radius of the capsule shell.

We averaged the image perpendicular to the direction of the modulations in a region indicated in Fig. 3. This produces an average intensity signal, I, in the direction across the modulations, as shown in the bottom of Fig. 3. The low modes (<5) from a Fourier decomposition of I were used to provide a baseline signal, I_B, also shown in the bottom of Fig. 3. The comparison of these signals gives a modulation in OD, $\Delta M = \log(I/I_B)$.

A sine curve was fitted to the resulting modulation amplitude signal, prioritizing the central two wavelengths that are in direct line of the x-ray imaging systems; an example is shown in Fig. 3. The wavelength of the sine fit is used to infer the radius of the capsules' cold shell, as the mode of the preimposed ripple remains constant during the compression. The amplitude of the fit is related to the total growth in OD of the ripple, from the initial ripple ΔM of 7.3×10^{-5} OD. This ΔM can be related to the total shell ρR if the opacity of the nonmodulated material in the shell is known.

The image processing also corrected for the modulation transfer function of the pinhole and MCP detector. This results in a correction factor to the amplitude inferred from the sine fit. Simulated radiographs, shown in Fig. 3, were processed in the same manner as the experimental data to allow direct comparison of the resulting inferred modulations.

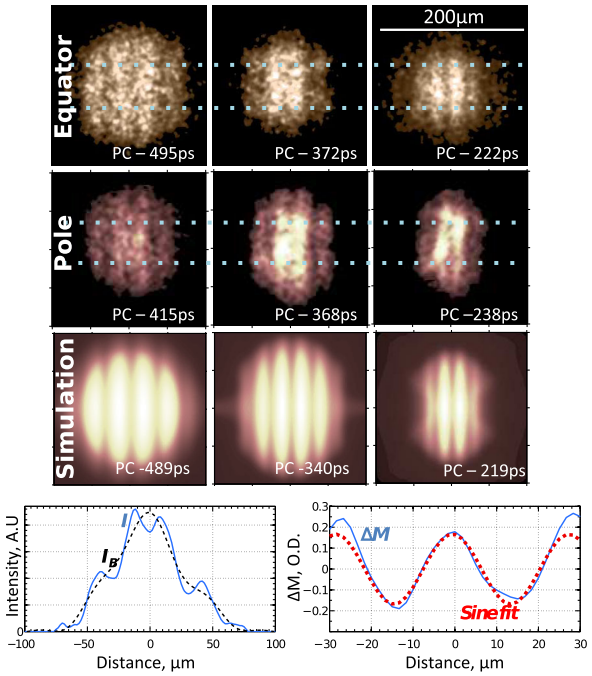

FIG. 3. A series of self-radiographs taken with a 12× magnification, 12 μm pinhole imaging system onto a GXD detector with ~100 ps temporal resolution through a 10 μm Cu filter, from the polar and equatorial line of sight, compared with the simulated self-radiographs attenuated by the same filtration and modulation transfer function as the experimental imaging system. The self-radiograph is formed by the hot rebounding shock self-emission being attenuated by the cold shell, which has the perturbations on its outer surface. The dotted lines indicate the region spatially averaged over to infer the preimposed modulation wavelength and amplitude as a function of time. An example of the analysis for the polar view, PC -368 ps, shows the signal I, solid blue, the self-emission from the rebound shock, I_B dashed black, on the left. The calculated modulation amplitude, solid blue, and sine fit, dashed red, is shown on the right.

Figure 4(a) shows the inferred radius, R, as a function of time for the polar, equatorial, and simulated self-radiographs. There is good agreement between the two lines of sight (LOS) and the simulation, showing a convergence velocity of (210 ± 15) km/s. The convergence inferred from the x-ray images increases from 4.6× ($R = 200$ μm) to 7.7× ($R = 120$ μm), which is in reasonable agreement with the estimate of convergence of $(5.1 \pm 0.2)\times$ obtained from the Cu dopant absorption feature in the time resolved spectrum. These are the highest convergence radiographs made of the shell at the NIF, providing improved knowledge of the late-time implosion dynamics.

Figure 4(b) shows the inferred ΔM as a function of the inferred radius for the pole, equator, and simulation. This shows that over the observation period the amplitude of the ripple continues to grow, but by different amounts on the equator and pole. During the time of our measurement, the continued increase in the ΔM for either location follows a $\sim 1/R^2$ dependence, consistent with the growth of $\rho \Delta R$

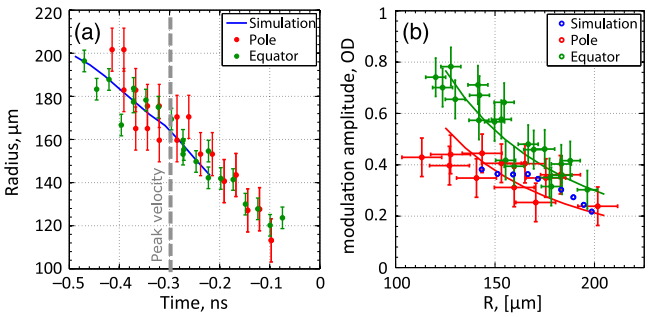

FIG. 4. (a) Radius vs time for experimental and simulated self-radiographs taken on the pole and equator. (b) Modulation amplitude vs radius for the pole and the equator showing continued growth of the modulation on both LOS with a difference in the measured growth between the equator and pole. Solid lines are proportional to $1/R^2$. The simulated radiographs use a 1D drive that is an average of the pole and equator. The initial modulation amplitude of the perturbation in the ablator was 7.3×10^{-5} OD.

mandated by mass conservation as a thin shell converges (i.e., the Bell-Plesset effect [24,25,61]) with no additional contribution from Rayleigh-Taylor growth. This is expected, since the Rayleigh-Taylor growth of our (110 ± 10) nm amplitude perturbation will reach saturation before the capsule reaches PV [54]. It is difficult to extrapolate the ΔM in OD measurement to a $\Delta \rho R$ as the material composition along the LOS is not experimentally known. The earliest measurements made on both the pole and equator overlap in error bars with the inferred OD from the simulated radiographs, which provide the best estimate for $\Delta \rho R$ at PV, the simulated $\Delta \rho R$ is $\simeq 0.5$ g/cm^2.

At the end of the set of analyzed images, the perturbation at the equator is seen to have grown twice as much in optical depth as on the pole. The difference in total growth observed on the equatorial and polar LOS is intriguing. The reduced growth at the pole may be due to more x-ray preheating originating from the laser beams that dominate the drive at the poles. Hydrodynamic growth at the ablator is sensitive to the gold M-band preheating and to the strength of the shocks as they traverse the shell. The observation of asymmetry in the M-band emission in hohlraums [62] and the dependence on shock strength of the ablative Richtmyer-Meshkov instability [13–17,63–65] have both been previously discussed as possible origins of asymmetric instability growth [61,66,67]. The self-radiograph technique opens new areas of research to measure the asymmetry in growth factors as the implosion remains unperturbed at PV.

In our experiment, the measured mode 40 perturbation grew by a factor of 0.6×10^4 to 1×10^4 in OD from the initial 7.3×10^{-5} OD of the (110 ± 10) nm amplitude ripple, to an amplitude of ~0.75 OD at the equator and ~0.42 OD at the pole, 100 ps prior to PC. Simulations indicate that a perturbation with 1/4 this initial amplitude would remain mostly in the linear regime and grow by a factor of 11 000.

We should therefore be able to measure mode 40 near PV arising from an initial amplitude of ~25 nm, comparable to perturbations from native roughness.

The shell ρR can be inferred from the time resolved spectroscopy and Ross pair imaging [68] that was fielded during these experiments; these will be discussed in a separate publication. Higher mode perturbations could soon be observed through the use of new high resolution imaging systems. Current 12 μm pinholes limit the observable modes at PV to those less than ~120. An ideal candidate to improve the measurements is the Kirkpatrick-Baez Microscope [69], recently demonstrated on the NIF [70,71] that combines <8 μm resolution imaging with narrow band energy responsiveness in addition to a larger photon collection efficiency when compared to similar resolution imaging systems. This diagnostic will improve the measurements discussed here, allowing higher modes and lower amplitudes to be measured.

The authors thank the engineering, target fabrication, and operations teams at the National Ignition Facility who made these experiments possible. This work was performed under the auspices of the U.S. Department of Energy by Lawrence Livermore National Laboratory under Contract No. DE-AC52-07NA27344.

*pickworth1@llnl.gov

[1] J. Nuckolls and L. Wood, Nature (London) **239**, 139 (1972).
[2] G. H. Miley, *Physics of Inertial Fusion: Beam Plasma Interaction, Hydrodynamics, Hot Dense Matter*, edited by S. Atzeni and J. Meyer-ter-vehn (Cambridge University Press, 2005).
[3] J. D. Lindl, *Inertial Confinement Fusion: The Quest for Ignition and Energy Gain Using Indirect Drive* (AIP Press, New York, 1998).
[4] V. A. Smalyuk, L. J. Atherton, L. R. Benedetti, R. Bionta, D. Bleuel, E. Bond, D. K. Bradley, J. Caggiano, D. A. Callahan, and D. T. Casey, Phys. Rev. Lett. **111**, 215001 (2013).
[5] M. J. Edwards, P. K. Patel, J. D. Lindl, L. J. Atherton, S. H. Glenzer, S. W. Haan, J. D. Kilkenny, O. L. Landen, E. I. Moses, and A. Nikroo, Phys. Plasmas **20**, 070501 (2013).
[6] G. H. Miller, E. I. Moses, and C. R. Wuest, Opt. Eng. (N.Y.) **43**, 2841 (2004).
[7] S. W. Haan, J. D. Lindl, D. A. Callahan, D. S. Clark, J. D. Salmonson, B. A. Hammel, L. J. Atherton, R. C. Cook, M. J. Edwards, and S. Glenzer, Phys. Plasmas **18**, 051001 (2011).
[8] J. L. Milovich, H. F. Robey, D. S. Clark, K. L. Baker, D. T. Casey, C. Cerjan, J. Field, A. G. MacPhee, A. Pak, and P. K. Patel, Phys. Plasmas **22**, 122702 (2015).
[9] S. P. Regan *et al.*, Phys. Rev. Lett. **111**, 045001 (2013).
[10] T. Ma, P. K. Patel, N. Izumi, P. T. Springer, M. H. Key, L. J. Atherton, L. R. Benedetti, D. K. Bradley, D. A. Callahan, and P. M. Celliers, Phys. Rev. Lett. **111**, 085004 (2013).
[11] J. W. Strutt, Proc. London Math. Soc. **14**, 170 (1883).
[12] G. Taylor, Proc. R. Soc. A **201**, 192 (1950).
[13] R. D. Richtmyer, Commun. Pure Appl. Math. **13**, 297 (1960).
[14] E. E. Meshkov, Fluid Dyn. **4**, 101 (1972).
[15] V. N. Goncharov, Phys. Rev. Lett. **82**, 2091 (1999).
[16] Y. Aglitskiy, A. L. Velikovich, M. Karasik, V. Serlin, C. J. Pawley, A. J. Schmitt, S. P. Obenschain, A. N. Mostovych, J. H. Gardner, and N. Metzler, Phys. Rev. Lett. **87**, 265001 (2001).
[17] T. Endo, K. Shigemori, H. Azechi, A. Nishiguchi, K. Mima, M. Sato, M. Nakai, S. Nakaji, N. Miyanaga, S. Matsuoka, A. Ando, K. A. Tanaka, and S. Nakai, Phys. Rev. Lett. **74**, 3608 (1995).
[18] O. V. Gotchev, V. N. Goncharov, J. P. Knauer, T. R. Boehly, T. J. B. Collins, R. Epstein, P. A. Jaanimagi, and D. D. Meyerhofer, Phys. Rev. Lett. **96**, 115005 (2006).
[19] W. Thomson, *Mathematical and Physical Papers* (Cambridge University Press, Cambridge, England, 1910), Vol. 4, p. 76.
[20] H. L. F. von Helmholtz, Wissenschaften zu Berlin **23**, 215 (1868).
[21] L. D. Landau and E. M. Lifshitz,*Course of Theoretical Mechanics: Fluid Mechanics* (Pergamon, 1959).
[22] S. Chandrasekhar, *Hydrodynamic and Hydromagnetic Stability* (Oxford University Press, Oxford, 1961).
[23] P. G. Drazin and W. H. Reid, *Hydrodynamic Stability* (Cambridge University Press, Cambridge, England, 2004).
[24] G. I. Bell, Los Alamos National Laboratory, Los Alamos, NM, Report No. LA-1321, 1951.
[25] M. S. Plesset and S. A. Zwick, J. Appl. Phys. **25**, 493 (1954).
[26] J. L. Peterson, D. T. Casey, O. A. Hurricane, K. S. Raman, H. F. Robey, and V. A. Smalyuk, Phys. Plasmas **22**, 056309 (2015).
[27] K. S. Raman, V. A. Smalyuk, D. T. Casey, S. W. Haan, D. E. Hoover, O. A. Hurricane, J. J. Kroll, A. Nikroo, J. L. Peterson, and B. A. Remington, Phys. Plasmas **21**, 072710 (2014).
[28] V. A. Smalyuk, D. T. Casey, D. S. Clark, M. J. Edwards, S. W. Haan, A. Hamza, D. E. Hoover, W. W. Hsing, O. Hurricane, J. D. Kilkenny, J. Kroll, O. L. Landen, A. Moore, A. Nikroo, L. Peterson, K. Raman, B. A. Remington, H. F. Robey, S. V. Weber, and K. Widmann, Phys. Rev. Lett. **112**, 185003 (2014).
[29] D. T. Casey *et al.*, Phys. Rev. E **90**, 011102 (2014).
[30] V. A. Smalyuk, M. Barrios, J. A. Caggiano, D. T. Casey, C. J. Cerjan, D. S. Clark, M. J. Edwards, J. A. Frenje, M. Gatu-Johnson, and V. Y. Glebov, Phys. Plasmas **21**, 056301 (2014).
[31] B. A. Hammel, S. W. Haan, D. S. Clark, M. J. Edwards, S. H. Langer, M. M. Marinak, M. V. Patel, J. D. Salmonson, and H. A. Scott, High Energy Density Phys. **6**, 171 (2010).
[32] V. A. Smalyuk, S. V. Weber, D. T. Casey, D. S. Clark, J. E. Field, S. W. Haan, B. A. Hammel, A. V. Hamza, D. E. Hoover, and O. L. Landen, Phys. Plasmas **22**, 072704 (2015).
[33] S. R. Nagel, S. W. Haan, J. R. Rygg, M. Barrios, L. R. Benedetti, D. K. Bradley, J. E. Field, B. A. Hammel, N. Izumi, and O. S. Jones, Phys. Plasmas **22**, 022704 (2015).
[34] R. Tommasini, J. E. Field, B. A. Hammel, O. L. Landen, S. W. Haan, C. Aracne-Ruddle, L. R. Benedetti, D. K. Bradley, D. A. Callahan, and E. L. Dewald, Phys. Plasmas **22**, 056315 (2015).

[35] S. W. Haan, H. Huang, M. A. Johnson, M. Stadermann, S. Baxamusa, S. Bhandarkar, D. S. Clark, V. Smalyuk, and H. F. Robey, Phys. Plasmas **22**, 032708 (2015).
[36] B. Yaakobi, R. L. McCrory, S. Skupsky, J. A. Delettrez, P. Bourke, H. Deckman, C. F. Hooper, and J. M. Soures, Opt. Commun. **34**, 213 (1980).
[37] D. K. Bradley, J. A. Delettrez, R. Epstein, R. P. J. Town, C. P. Verdon, B. Yaakobi, S. Regan, F. J. Marshall, T. R. Boehly, and J. P. Knauer, Phys. Plasmas **5**, 1870 (1998).
[38] B. Yaakobi, V. A. Smalyuk, J. A. Delettrez, F. J. Marshall, D. D. Meyerhofer, and W. Seka, Phys. Plasmas **7**, 3727 (2000).
[39] V. A. Smalyuk, V. N. Goncharov, J. A. Delettrez, F. J. Marshall, D. D. Meyerhofer, S. P. Regan, and B. Yaakobi, Phys. Rev. Lett. **87**, 155002 (2001).
[40] V. A. Smalyuk, J. A. Delettrez, V. N. Goncharov, F. J. Marshall, D. D. Meyerhofer, S. P. Regan, T. C. Sangster, R. P. J. Town, and B. Yaakobi, Phys. Plasmas **9**, 2738 (2002).
[41] T. R. Boehly, R. S. Craxton, T. H. Hinterman, J. H. Kelly, T. J. Kessler, S. A. Kumpan, S. A. Letzring, R. L. McCrory, S. F. B. Morse, and W. Seka, Rev. Sci. Instrum. **66**, 508 (1995).
[42] H. M. Johns, R. C. Mancini, P. Hakel, T. Nagayama, V. A. Smalyuk, S. P. Regan, and J. Delettrez, Phys. Plasmas **21**, 082711 (2014).
[43] S. P. Regan *et al.*, Phys. Rev. Lett. **89**, 085003 (2002).
[44] D. D. Meyerhofer, J. A. Delettrez, R. Epstein, V. Y. Glebov, V. N. Goncharov, R. L. Keck, R. L. McCrory, P. W. McKenty, F. J. Marshall, and P. B. Radha, Phys. Plasmas **8**, 2251 (2001).
[45] B. Yaakobi, R. S. Craxton, R. Epstein, and Q. Su, J. Quant. Spectrosc. Radiat. Transfer **58**, 75 (1997).
[46] V. A. Smalyuk, S. B. Dumanis, F. J. Marshall, J. A. Delettrez, D. D. Meyerhofer, S. P. Regan, T. C. Sangster, B. Yaakobi, and J. A. Koch, Phys. Plasmas **10**, 830 (2003).
[47] V. A. Smalyuk, J. A. Delettrez, S. B. Dumanis, V. Y. Glebov, V. N. Goncharov, J. P. Knauer, F. J. Marshall, D. D. Meyerhofer, P. B. Radha, and S. P. Regan, Phys. Plasmas **10**, 1861 (2003).
[48] J. A. Koch, T. W. Barbee Jr, N. Izumi, R. Tommasini, R. C. Mancini, L. A. Welser, and F. J. Marshall, Rev. Sci. Instrum. **76**, 073708 (2005).
[49] L. Welser-Sherrill, R. C. Mancini, J. A. Koch, N. Izumi, R. Tommasini, S. W. Haan, D. A. Haynes, I. E. Golovkin, J. J. MacFarlane, J. A. Delettrez, F. J. Marshall, S. P. Regan, V. A. Smalyuk, and G. Kyrala, Phys. Rev. E **76**, 056403 (2007).
[50] T. Nagayama, R. C. Mancini, R. Florido, R. Tommasini, J. A. Koch, J. A. Delettrez, S. P. Regan, and V. A. Smalyuk, J. Appl. Phys. **109**, 093303 (2011).
[51] T. Nagayama, R. C. Mancini, R. Florido, D. Mayes, R. Tommasini, J. A. Koch, J. A. Delettrez, S. P. Regan, and V. A. Smalyuk, Phys. Plasmas **21**, 050702 (2014).
[52] R. C. Mancini, C. F. Hooper, and R. L. Coldwell, J. Quant. Spectrosc. Radiat. Transfer **51**, 201 (1994).
[53] B. A. Hammel, V. A. Smalyuk, T. Doeppner, S. W. Haan, T. Ma, L. Pickworth, and H. A. Scott, in BAPS.2013.DPP.NP8.108 (2013).
[54] S. W. Haan, Phys. Fluids B **3**, 2349 (1991).
[55] M. M. Marinak, G. D. Kerbel, N. A. Gentile, O. Jones, D. Munro, S. Pollaine, T. R. Dittrich, and S. W. Haan, Phys. Plasmas **8**, 2275 (2001).
[56] F. Pérez, G. E. Kemp, S. P. Regan, M. A. Barrios, J. Pino, H. Scott, S. Ayers, H. Chen, J. Emig, and J. D. Colvin, Rev. Sci. Instrum. **85**, 11D613 (2014).
[57] M. A. Barrios, D. A. Liedahl, M. B. Schneider, O. Jones, G. V. Brown, S. P. Regan, K. B. Fournier, A. S. Moore, J. S. Ross, and O. Landen, Phys. Plasmas **23**, 056307 (2016).
[58] B. L. Henke, E. M. Gullikson, and J. C. Davis, Atomic Data Nucl. Data Tables **54**, 181 (1993).
[59] J. Park, G. V. Brown, M. B. Schneider, H. A. Baldis, P. Beiersdorfer, K. V. Cone, R. L. Kelley, C. A. Kilbourne, E. W. Magee, and M. J. May, Rev. Sci. Instrum. **81**, 10E319 (2010).
[60] L. R. Benedetti, J. P. Holder, M. Perkins, C. G. Brown, C. S. Anderson, F. V. Allen, R. B. Petre, D. Hargrove, S. M. Glenn, and N. Simanovskaia, Rev. Sci. Instrum. **87**, 023511 (2016).
[61] V. N. Goncharov, P. McKenty, S. Skupsky, R. Betti, R. L. McCrory, and C. Cherfils-Clérouin, Phys. Plasmas **7**, 5118 (2000).
[62] W. S. Varnum, N. D. Delamater, S. C. Evans, P. L. Gobby, J. E. Moore, J. M. Wallace, R. G. Watt, J. D. Colvin, R. Turner, V. Glebov, J. Soures, and C. Stoeckl, Phys. Rev. Lett. **84**, 5153 (2000).
[63] Y. Aglitskiy, A. L. Velikovich, M. Karasik, V. Serlin, C. J. Pawley, A. J. Schmitt, S. P. Obenschain, A. N. Mostovych, J. H. Gardner, and N. Metzler, Phys. Plasmas **9**, 2264 (2002).
[64] N. Metzler, A. L. Velikovich, and J. H. Gardner, Phys. Plasmas **6**, 3283 (1999).
[65] A. G. MacPhee, D. T. Casey, D. S. Clark, O. S. Jones, J. L. Milovich, J. L. Peterson, H. F. Robey, and V. A. Smalyuk, Phys. Rev. Lett. (to be published).
[66] J. L. Peterson, D. S. Clark, L. P. Masse, and L. J. Suter, Phys. Plasmas **21**, 092710 (2014).
[67] B. Motl, J. Oakley, D. Ranjan, C. Weber, M. Anderson, and R. Bonazza, Phys. Fluids **21**, 126102 (2009).
[68] N. Izumi, T. Ma, M. Barrios, L. R. Benedetti, D. Callahan, C. Cerjan, J. Edwards, S. Glenn, S. Glenzer, and J. Kilkenny, Rev. Sci. Instrum. **83**, 10E121 (2012).
[69] P. Kirkpatrick and A. V. Baez, J. Opt. Soc. Am. **38**, 766 (1948).
[70] L. A. Pickworth, T. McCarville, T. Decker, T. Pardini, J. Ayers, P. Bell, D. Bradley, N. F. Brejnholt, N. Izumi, P. Mirkarimi, M. Pivovaroff, V. Smalyuk, J. Vogel, C. Walton, and J. Kilkenny, Rev. Sci. Instrum. **85**, 11D611 (2014).
[71] N. F. Brejnholt, J. J. Ayers, T. J. McCarville, T. Pardini, L. A. Pickworth, D. K. Bradley, T. A. Decker, S. P. Hau-Riege, R. M. Hill, and M. J. Pivovaroff, Proc. SPIE **9591**95910J (2015).